nature materials

Supplementary information

https://doi.org/10.1038/s41563-025-02462-w

Cell viscosity influences haematogenous dissemination and metastatic extravasation of tumour cells

In the format provided by the authors and unedited

Supplementary Information (SI) table of content:

Supplementary Text:

AFM-based rheology of siRNA-treated D2A1 tumor cells

Because intravascular arrest could potentially impact the mechanics of tumor cells as they might initiate intravascular adhesion and spreading, we used AFM-based rheology to check whether cells in early adhesion / spreading stages might undergo cytoskeletal rearrangements that would invalidate our MPA measurements. We probed the mechanical properties of the cortex of cells that were left to initiate adhesion / spreading on fibronectin for one hour (Supplementary fig. 5a-b), and found that all-but-one (siCAV1) treatments decreased the shear storage G' (Supplementary fig. 5c-d), which accounts for cortex elasticity, and decreased the shear loss G" (Supplementary fig. 5e-f), which accounts for cortex viscosity[47]. Interestingly, depleting MYH9 led to increased loss tangent G"/G' (ratio of viscous / elastic regime) confirming our initial observation on whole-cell mechanics of cells in suspension that such treatment disrupts elasticity more so than it affects viscosity (Supplementary fig. 5g-h). Despite a slight discrepancy in mechanical profiling (MPA vs AFM) observed for siCAV1-treated cells, we thus further validated that the initial mechanical perturbations of cells would mostly be conserved in the event that they would start adhering and spreading.

Supplementary methods:

Western Blot

Protein extractions were performed with homemade RIPA buffer. Protein concentrations of the extracts were first quantified using a Bradford assay, and equal protein quantities were then loaded on 4-20% polyacrylamide gels (Biorad) or 4-20% Tris-Glycine gels (Introvigen) and run under denaturing conditions. The following primary antibodies were used: Anti-vimentin (D21H3, Cell Signaling), Anti-lamin A/C (sc-7292 and sc-20681, Santa Cruz), Anti-non-muscle myosin IIA (M8064, Sigma), Anti-caveolin-1 (D46G3, Cell Signaling), Anti-transgelin (ab14106, Abcam), Anti-GAPDH (MAB374, Merck Millipore).

In vitro live adhesion assay

Quantification of the flow-dependent adhesion of CTCs was done using six channels µ-slides VI^{0,4} Luer (IBIDI) as previously described[69]. Briefly, channels were coated with bovine plasma fibronectin at 10 µg/ml (Sigma). HUVEC cells were seeded at 30 000 cells per channel. Medium was changed twice a day until they reach maximal confluency (3-4 days). Three days after siRNA transfection, D2A1 tumor cells were resuspended at a concentration of 10^6 cells/ml. Cells were perfused using a REGLO Digital MS-2/12 peristaltic pump (Ismatec), Tygon LMT-55 3-stop tubing (IDEX), 0.5- and 1.6-mm silicon tubing and elbow Luer connectors (IBIDI). For live imaging, the HUVEC medium was supplemented with 20 mM HEPES. D2A1 adhesion was imaged for 2 minutes at different speeds using a Leica DMIRE2 inverted microscope equipped with a 20X objective (Leica), a USB 3.0 µEye IDS CCD camera (IDEX) and a 37°C heating chamber.

In vitro clustering assay

siRNA-treated D2A1 tumor cells were detached, centrifuged, resuspended in regular media and incubated for 2h on a rocker placed in an incubator (37°C, 5% CO2). Cells were then imaged with a 10X objective in non-adherent dishes. The epithelial 4T1 tumor cell line was used as a highly-clustering epithelial-like control while the B16F10 tumor cell line was used as minimally-clustering mesenchymal-like control.

RNA-sequencing

RNA integrity was assessed by Bioanalyzer (total RNA Pico Kit, 2100 Instrument, Agilent Technologies, Paolo Alto, CA, USA). All samples had RNA integrity numbers above 8 and DV200>80%. Sequencing libraries were prepared using “NEBNext Ultra II Directional RNA Library Prep Kit for Illumina“ and enriched in mRNA using “NEB Ultra II polyA mRNA magnetic isolation” kit (New England Biolabs, Ipswich, MA, USA). Libraries were pooled and sequenced (single-end, 100bp) on a NextSeq2000 according to the manufacturer’s instructions (Illumina Inc., San Diego, CA, USA). For each sample, quality control was carried out and assessed with the NGS Core Tools FastQC[70]. Sequence reads (minimum 48,5 million) were mapped to *Mus musculus* mm10 using STAR[71] to obtain a BAM (Binary Alignment Map) file. An abundance matrix was generated based on read counts identified by Featurecounts[72]. At last, differential expression analyses were performed using the DESeq2[73] package of the Bioconductor framework for RNASeq Data[74]. Up and down-regulated genes were selected based on the adjusted p-value (< 0.05) and the fold-change (> 1.5). Raw RNAseq Data have been deposited in the EMBL-EBI ArrayExpress archive (accession number E-MTAB-14571).

Multidimensional scaling (MDS) was performed on gene expression counts normalized using the DESeq2 R package[73]. MDS coordinates were calculated using the plotMDS function from the limma R package[75]. This function calculates pairwise distances between samples based on their expression profiles. The top two dimensions were retained for visualization, representing the major sources of variation in the Dataset, typically reflecting biological or technical differences between samples.

Atomic Force Microscopy (AFM)-based rheology

Suspended siRNA-treated D2A1 tumor cells were plated on a fibronectin-coated tissue culture dish (FluoroDish, WPI) and placed in an incubator for 1 h at 37°C and 5% CO_2 to let the cells adhere. Dishes were then mounted on a combined AFM (NanoWizard5, Bruker) and inverted microscope (Observer, Zeiss) setup. To maintain the cells at culture conditions (37°C and 5% CO_2) during the experiment, the setup was kept in a temperature-controlled chamber (The Cube, Life Imaging Services) and the dish with 2 ml of usual culture medium was perfused with a humified gas mixture comprising synthetic air with 5% CO_2 [76]. A bead with diameter of 5 µm (Kisker Biotech, PSI-5.0)

was glued to the free end of a triangular cantilever (NPO-D, Bruker, nominal spring constant 0.06 N m^{-1}) prior to the experiment. To measure the rheological properties of the cells, the bead was indented at 10 µm s^{-1} on top of the nuclei of single cells until reaching a setpoint of 1 nN and oscillated at frequencies of 4.5, 10, 22, 45 and 100 Hz with an amplitude of 10 nm, as per measurement principle established in prior work[77]. The resulting average cell indentation mean was 2 µm. The rheological Data was analyzed with Bruker software (DP Version 8.0.157).

Supplementary discussion:

In this study, we demonstrate that cell mechanics, in particular viscosity, is pivotal during hematogenous dissemination of CTCs, impacting their circulation, arrest, and extravasation. Specifically, low viscosity facilitates CTC entry and lodging in constraining capillary-sized vessels. In contrast, high viscosity promotes endothelial remodeling and supports extravasation that precedes metastatic outgrowth.

We circumvented the lack of reliable mechanical profiling methods *in vivo* by using polyacrylamide beads[24] that can mimic the size and elasticity of cells when injected in zebrafish embryos. While they mostly exhibit elastic behavior[48], they allowed us to demonstrate that mechanical properties (size, elasticity) of circulating objects control their circulation and arrest patterns. When zooming into occlusion hotspots, we exploited their potential in sensing stress based on their deformation[25,49,50] and realized that they surprisingly displayed only minimal shape changes upon arrest in constraining vessels. This was in sharp contrast with CTC whose morphological changes scaled with vascular constraints. As viscosity properties cannot be modelled by elastic polyacrylamide beads (≈ 0.8 kPa), we hypothesized that cellular viscosity was the underappreciated property allowing cells to navigate in constraining vessels. This was confirmed by passivating cells via ATP depletion which further demonstrated that cells exhibit fluid-like behaviour to reach constraining environments. Designing cell-mimicking viscoelastic beads[48] compatible with *in vivo* experimental settings will be key for further appreciating the role of cell mechanics in disease.

We approached the respective contributions of elasticity and viscosity in a realistic tumor cell model by i) modulating key nodes of cell mechanics[51], 2024) : lamin A/C[52], vimentin[53], caveolin-1[54], non-muscle myosin IIA[55], transgelin[56] and by 2) comparing pairs of patient-derived cell lines, with similar background but different mechanical phenotypes. We mitigated the drawbacks of both approaches notably by monitoring potential collateral effects of the RNAi treatments on gene expression, cell adhesion and clustering, as these features may influence the fate of CTCs[12,13,57]. Patient-derived cell lines were carefully selected to represent different cancer types (breast, colon and skin cancer), stages of the diseases (CTC vs metastatic) and resistance to treatments[27–29,58].

We find that whole-cell viscosity is highly influenced by nuclear mechanics and impacts the entire metastatic process by favoring lodging in small constraining vessels, which is central in metastatic organ colonization[14,59]. Once arrested, metastatic success depends i) on the survival of the cells, that often suffer from intravascular fragmentation[23] that could potentially arise because of a non-compliant viscous profile, and ii) on their ability to extravasate. Although extravasation dynamics and efficiency differ between animal models and are thus likely to differ significantly in humans, we found that low viscosity may indirectly promote metastatic progression by enabling rapid extravasation from the hostile intravascular environment and its hemodynamic forces[2,7]. Some tumor cells exploit an endothelium-assisted process (in ZF embryos[15,30]; in a model of mouse brain metastasis[22]) which hijacks a mechanism meant to recanalize occluded microvessels[60]. As such event mostly occurs in capillaries, one might speculate that the process might be triggered more quickly in small vessels where full occlusion is frequent. Strikingly, low viscosity tumor cells displayed a significant decrease in endothelial-based extravasation efficiency, suggesting that the endothelial remodeling process, which we previously found to be mechanosensitive to hemodynamic forces[15,30], might also be sensitive to the mechanical properties of the occluding arrested object: High viscosity cells could be more likely to resist undergoing large deformation and instead induce significant deformation of the endothelium, much like purely elastic arrested beads induced reshaping of the endothelium around them instead of themselves adapting their shapes to the vessels in our bead imaging experiments. The observations that (1) extravasation phenotypes correlated more with whole-cell mechanics as measured by MPA than with cortex mechanics as measured by AFM, (2) arrested tumor cells consistently maintained a rounded shape without intravascular spreading until full extravasation was achieved, and (3) the process occurred more rapidly in smaller vessels where complete occlusion is more likely, further support the hypothesis that the extravasation process is predominantly influenced by the presence of the entire tumor cell entity and its whole-cell mechanical properties rather than localized mechanical properties of the cell cortex at adhesion interfaces.

The complexity of endothelial remodeling-driven extravasation is not limited to just these mechanical considerations but instead also likely lies in its heavy reliance on molecular features of the cells involved, as hinted by the absence of remodeling around beads or around the CTC-45 / CPP-45 cell line pair that we tested, as well as

some of our previous work on the importance of the adhesion repertoire in this process[13]. Undeniably, metastatic extravasation is a highly complex process, for which different mechanisms and timelines exist for different tumor cell lines. With our work, we provide novel insights into the contribution of cell viscosity in endothelium-assisted extravasation, suggesting that targeting cell mechanics (i.e. viscosity) could offer new therapeutical perspectives for impairing metastatic extravasation.

Metastatic outgrowth and success heavily rely on post-extravasation behavior of tumor cells, which face additional challenges that steer dormancy or proliferation phenotypes[61] that are likely additionally dependent on mechanics or mechanics-controlled events. While probing mechanics of such events remains impossible, we used a syngeneic whole-animal and mostly *ex vivo* mouse lung metastasis model and confirmed the reduced extravasation efficiency of low viscosity cells. Indeed, depleting vimentin led to increased outgrowth, in line with previous work that highlighted its repressing role in the context of TNBC[62]. Depletion of A-type lamins led to similar outgrowth-promoting effects in our model, in line with past work in which lower A-type lamin levels were found to correlate with increased metastatic potential in breast cancer[63]. However, this also contrasts with other work in which higher levels of A-type lamins were found to increase survivability and metastatic potential[64]. This further reinforces the notion that the contribution of mechanics to metastasis is complex, and highlights the need to better dissect the impact of purely mechanical vs other biological effects tied to cell mechanics nodes (e.g. the signalling scaffolding of vimentin[65] or the potential regulation of cellular functions downstream of nucleus deformation[66]) on the post-extravasation fate of tumor cells. In the context of our results, two hypotheses might explain low-viscosity tumor cells giving rise to bigger metastatic foci in spite of their extravasation defect : 1) The fact that low viscosity cells seed capillary networks in greater numbers might largely compensate for the extravasation defect ; and 2) A low viscosity mechanical phenotype might be linked to increased fitness to proliferate after extravasation completion and tissue colonization, as such links between mechanical softness and increased stemness and tumorigenicity would not be unprecedented[67]. Future work would benefit from the emergence of reliable *in vivo* mechanical profiling methods[68].

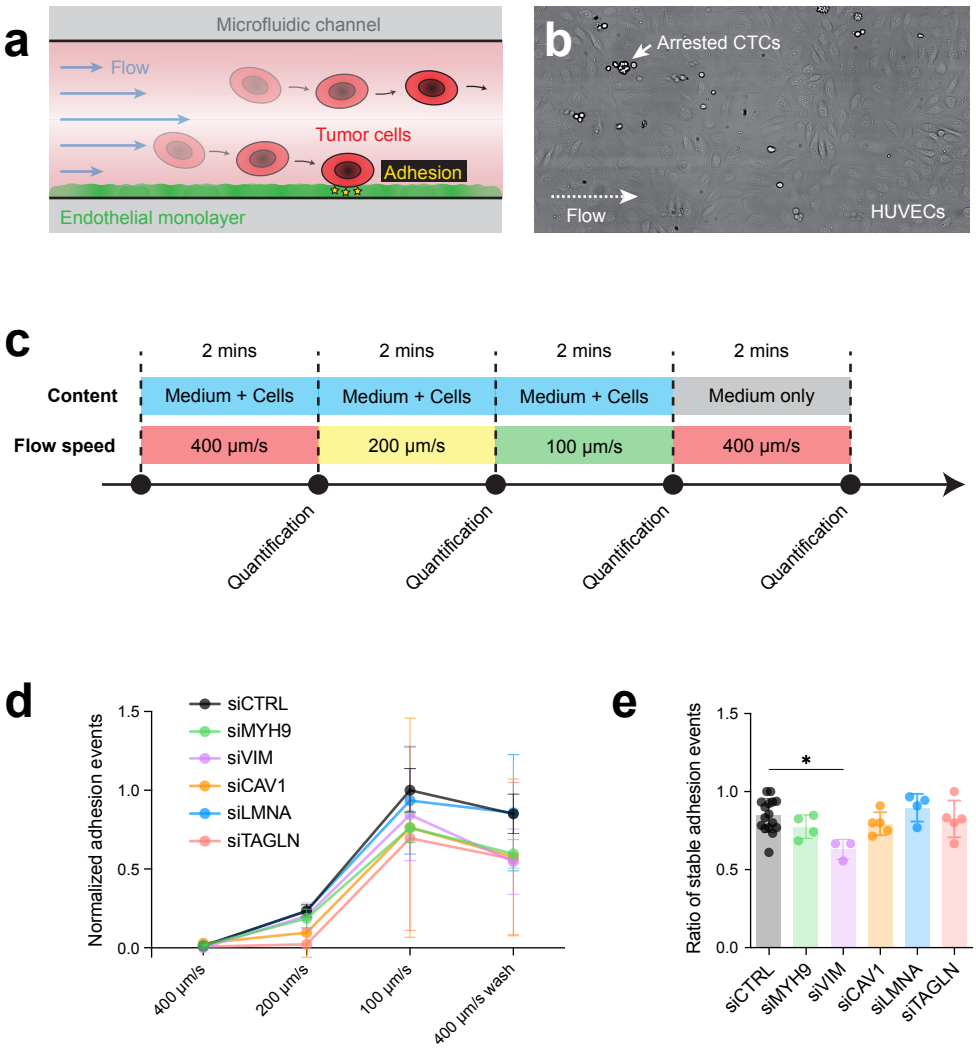

Supplementary Fig. 1: Live adhesion assay of siRNA-treated D2A1 tumor cells.
(a) Microfluidic setup for real-time in vitro adhesion assay. **(b)** Image of CTCs arrested in the HUVEC-coated microfluidic channel. **(c)** Protocol applied for assessing first-time adhesion abilities and adhesion stability of CTCs. **(d)** Quantification of ratio of adhesion events of siRNA-treated D2A1 tumor cells perfused in HUVEC-coated microfluidic channel. (N (populations of cells perfused) = 16 (siCTRL), 4 (siMYH9, siLMNA), 3 (siVIM) and 5 (siCAV1)) (2-way ANOVA of curves, Šidák's multiple comparisons test , p-values for 400 µm/s = > 0.9999 (all comparisons) ; p-values for 200 µm/s = > 0.9999 (siCTRL vs siVIM and siCTRL vs siLMNA), 0.9998 (siCTRL vs siMYH9), 0.9536 (siCTRL vs siCAV1), 0.7693 (siCTRL vs siTAGLN) ; p-values for 100 µm/s = 0.7459 (siCTRL vs siMYH9), 0.9658 (siCTRL vs siVIM), 0.6733 (siCTRL vs siCAV1), 0.9989 (siCTRL vs siLMNA), 0.4149 (siCTRL vs siTAGLN) ; p-values for 400 µm/s wash = 0.6947 (siCTRL vs siMYH9), 0.6362 (siCTRL vs siVIM), 0.5362 (siCTRL vs siCAV1), > 0.9999 (siCTRL vs siLMNA), 0.4785 (siCTRL vs siTAGLN)). **(e)** Quantification of ratio of stable adhesion (100 µm/s to 400 µm/s wash change) of siRNA-treated D2A1 tumor cells perfused in HUVEC-coated microfluidic channel. (N (populations of cells perfused) = 16 (siCTRL), 4 (siMYH9, siLMNA), 3 (siVIM) and 5 (siCAV1)) (Kruskal-Wallis followed by original FDR method of Benjamini and Hochberg, q-values = 0.4891 (siCTRL vs siMYH9), 0.0296 (siCTRL vs siVIM), 0.4891 (siCTRL vs siCAV1), 0.5064 (siCTRL vs siLMNA), 0.7563 (siCTRL vs siTAGLN)).

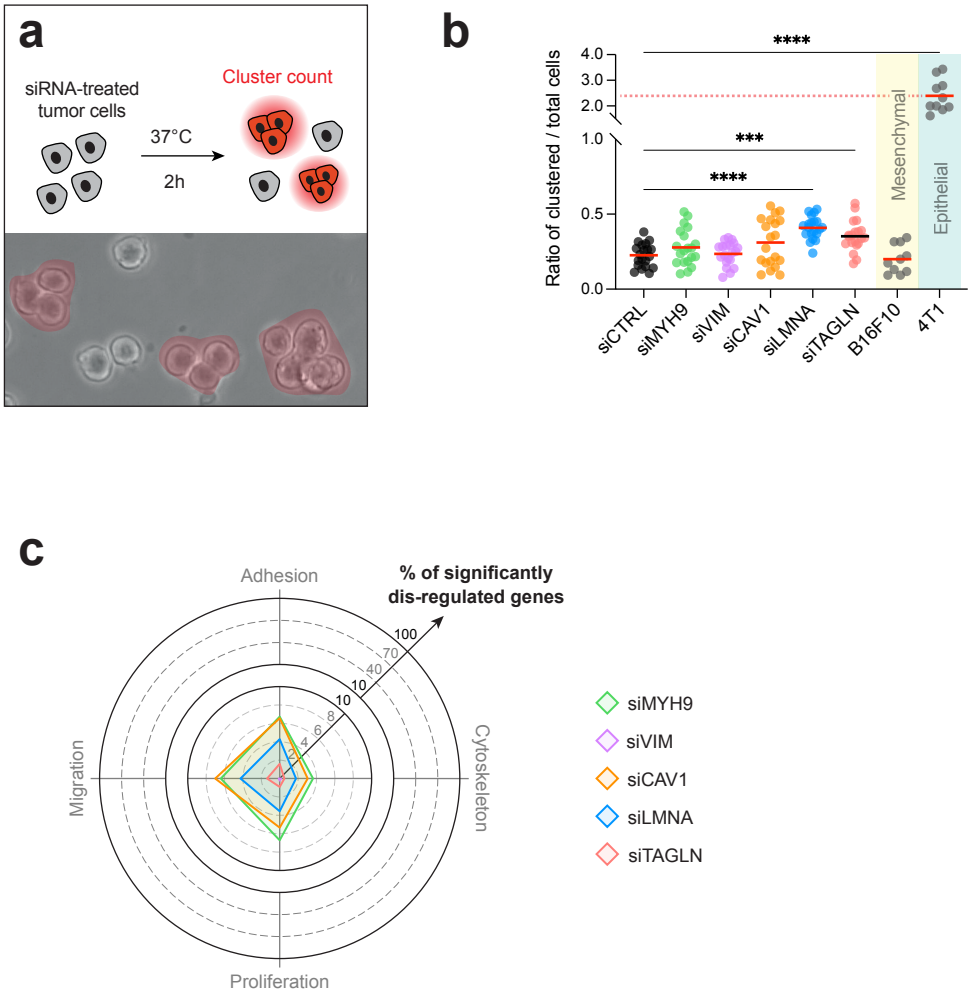

Supplementary Fig. 2: Effects of siRNA treatments on cell clustering and on expression of genes related to biological functions relevant to cancer cell behaviour.

(a) Protocol for in vitro clustering abilities assessment of siRNA-treated D2A1 tumor cells. **(b)** Quantification of ratio of clustered / total cells after 2 hours of incubation for siRNA-treated D2A1 tumor cells. B16F10 and 4T1 serve as mesenchymal and epithelial controls respectively. (N = 1, n (fields of view) = 20 (siCTRL, siMYH9, siVIM, siCAV1, siLMNA and siTAGLN), 10 (B16F10 and 4T1)) ((Kruskal-Wallis followed by original FDR method of Benjamini and Hochberg, q-values = 0.7581 (siCTRL vs B16F10) ; < 0.0001 (siCTRL vs 4T1) ; 0.3103 (siCTRL vs siMYH9) ; 0.7581 (siCTRL vs siVIM), 0.0910 (siCTRL vs siCAV1), < 0.0001 (siCTRL vs siLMNA), 0.0038 (siCTRL vs siTAGLN)). **(c)** Radar graph displaying percentage of genes of 4 gene signatures (adhesion, cytoskeleton, proliferation or migration) that are significantly dis-regulated in siRNA-treated D2A1 tumor cells compared to control. (N =1, n (number of genes analyzed) = 2262 (siMYH9 - Cytoskeleton), 2040 (siVIM - Cytoskeleton), 2201 (siCAV1, siLMNA - Cytoskeleton), 2155 (siTAGLN - Cytoskeleton), 1114 (siMYH9 - Adhesion), 903 (siVIM - Adhesion), 1051 (siCAV1, siLMNA - Adhesion), 1002 (siTAGLN - Adhesion), 1156 (siMYH9 - Migration), 1016 (siVIM - Migration), 1126 (siCAV1, siLMNA - Migration), 1096 (siTAGLN - Migration), 1504 (siMYH9 - Proliferation), 1323 (siVIM - Proliferation), 1461 (siCAV1, siLMNA - Proliferation), 1426 (siTAGLN - Proliferation)).

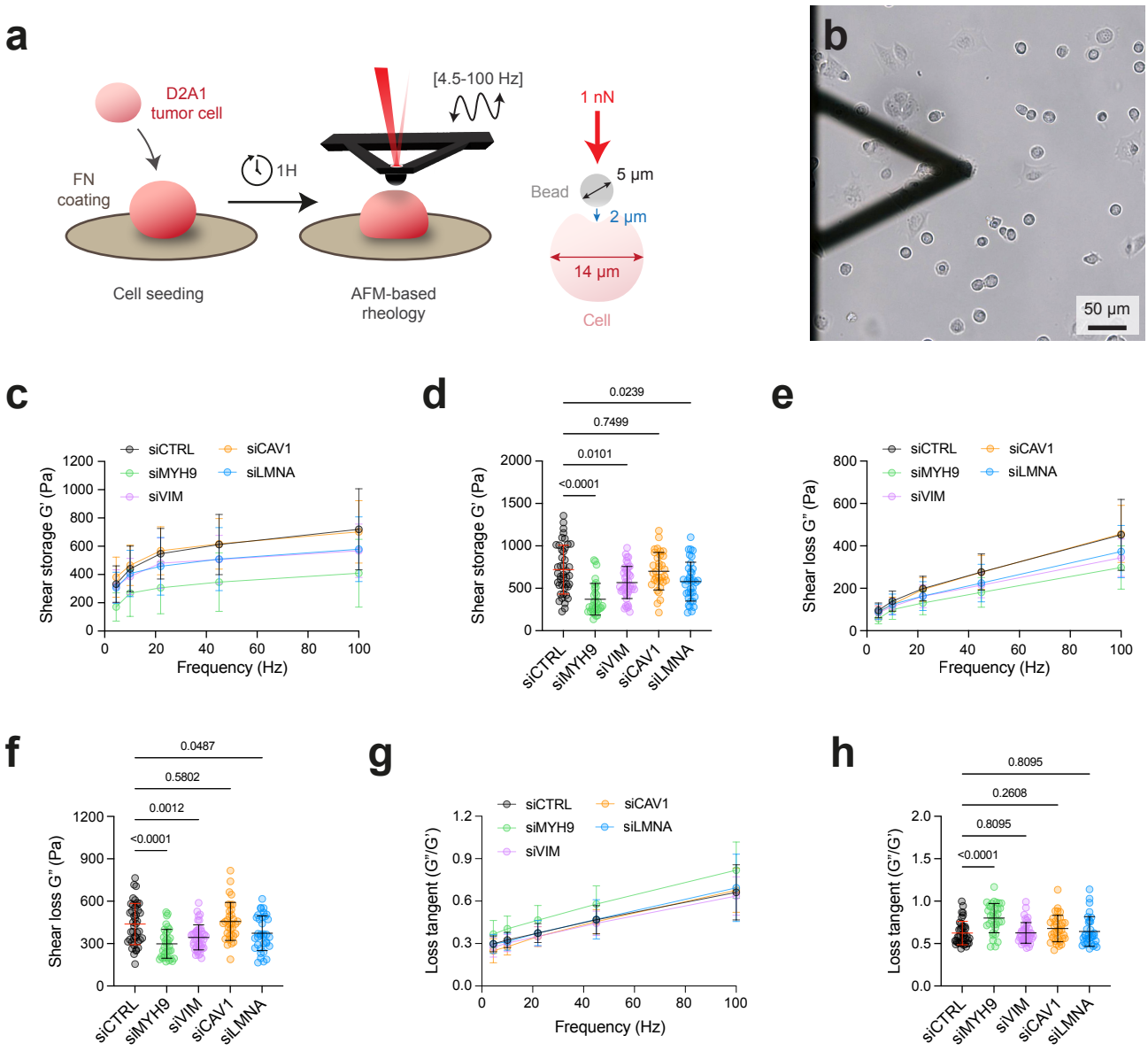

Supplementary Fig. 3: Rheological measurements of siRNA-treated tumor cells.
(a) Experimental setting for rheological measurements of tumor cells in the early spreading stage. **(b)** Representative DIC image of tumor cells 1 h post-seeding ready for AFM-based rheological measurements. **(c)** Shear storage (G') of siRNA-treated D2A1 tumor cells. Data points represent averages and vertical error bars represent standard deviations. (N = 3 (siCTRL, siMYH9, siVIM, siCAV1, siLMNA), n (cells) = 43 (siCTRL), 34 (siMYH9), 42 (siVIM), 33 (siCAV1), 35 (siLMNA)). **(d)** Shear storage (G') at 100 Hz oscillation frequency of siRNA-treated D2A1 tumor cells. (N = 3 (siCTRL, siMYH9, siVIM, siCAV1, siLMNA), n (cells) = 43 (siCTRL), 34 (siMYH9), 42 (siVIM), 33 (siCAV1), 35 (siLMNA)) (Brown-Forsythe and Welch ANOVA followed by original FDR method of Benjamini and Hochberg). **(e)** Shear loss (G") of siRNA-treated D2A1 tumor cells. Data points represent averages and vertical error bars represent standard deviations. (N = 3 (siCTRL, siMYH9, siVIM, siCAV1, siLMNA), n (cells) = 43 (siCTRL), 34 (siMYH9), 42 (siVIM), 33 (siCAV1), 35 (siLMNA)). **(f)** Shear loss (G") at 100 Hz oscillation frequency of siRNA-treated D2A1 tumor cells. (N = 3 (siCTRL, siMYH9, siVIM, siCAV1, siLMNA), n (cells) = 43 (siCTRL), 34 (siMYH9), 42 (siVIM), 33 (siCAV1), 35 (siLMNA)) (Brown-Forsythe and Welch ANOVA followed by original FDR method of Benjamini and Hochberg). **(g)** Loss tangent (G"/G') of siRNA-treated D2A1 tumor cells. Data points represent averages and vertical error bars represent standard deviations. (N = 3 (siCTRL, siMYH9, siVIM, siCAV1, siLMNA), n (cells) = 43 (siCTRL), 34 (siMYH9), 42 (siVIM), 33 (siCAV1), 35 (siLMNA)). **(h)** Loss tangent (G"/G') at 100 Hz oscillation frequency of siRNA-treated D2A1 tumor cells. (N = 3 (siCTRL, siMYH9, siVIM, siCAV1, siLMNA), n (cells) = 43 (siCTRL), 34 (siMYH9), 42 (siVIM), 33 (siCAV1), 35 (siLMNA)) (Kruskal-Wallis followed by original FDR method of Benjamini and Hochberg).

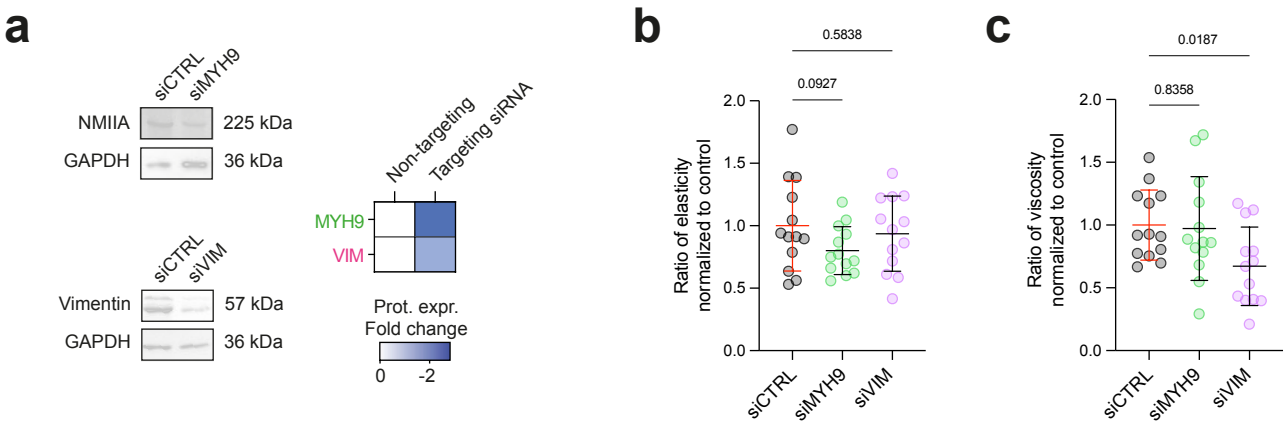

Supplementary Fig. 4: 7 days post-transfection effects of siRNA treatments.
(a) Representative WB images of protein expression of target-proteins 7 days post-transfection with siRNA and resulting protein expression fold changes. GAPDH loading controls were run on a separate gel in the NMIIA experiment. **(b)** Ratio of elasticity of siRNA-treated D2A1 tumor cells 7 days post-transfection normalized to control. (N = 1, n = 13 for siCTRL, siVIM and siMYH9) (Ordinary one- way ANOVA followed by original FDR method of Benjamini and Hochberg). **(c)** Ratio of viscosity of siRNA-treated D2A1 tumor cells 7 days post-transfection normalized to control. (N = 1, n = 13 for siCTRL, siVIM and siMYH9) (Ordinary one- way ANOVA followed by original FDR method of Benjamini and Hochberg).

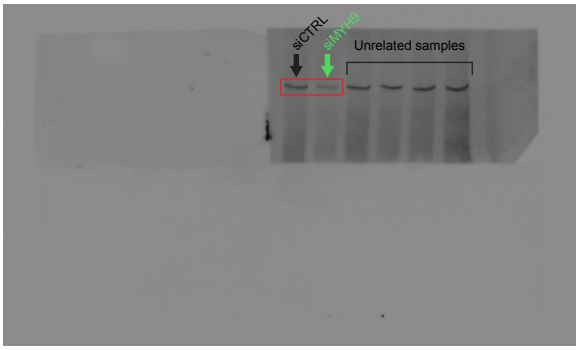

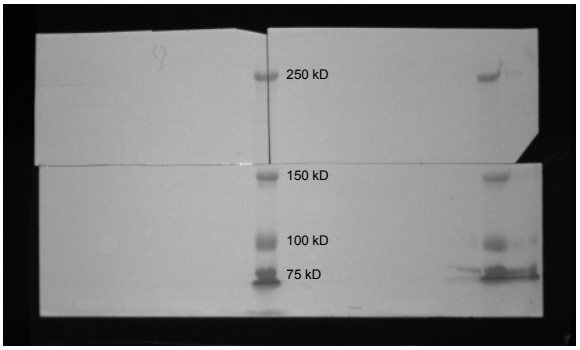

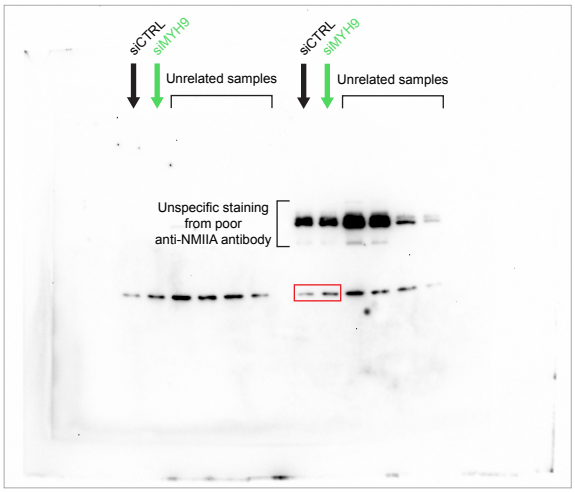

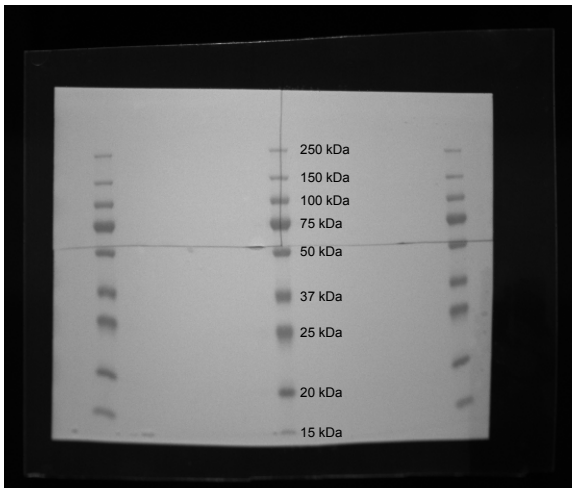

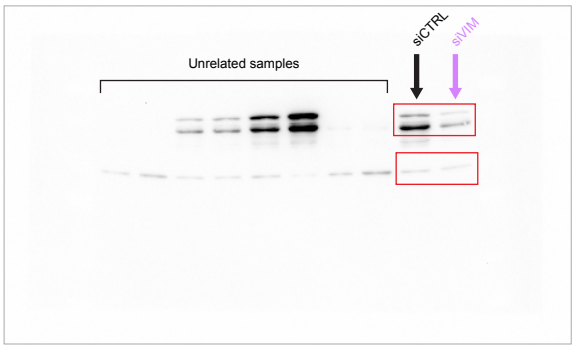

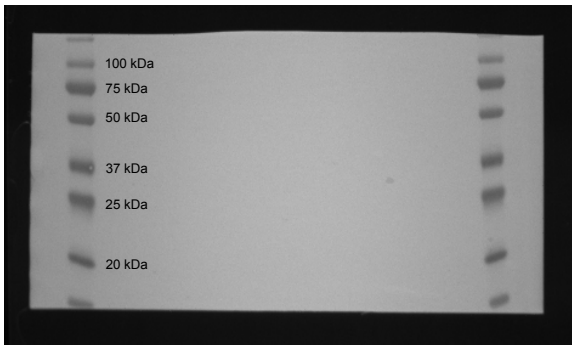

Additional Supplementary Figure:
Uncropped images of western blot bands used in Supplementary Fig. 4a. Red squares indicate cropped areas displayed in Supplementary Fig. 4a. N (WB) = 2 (NMIIA blots), 1 (Vimentin blots), n (protein extractions) = 1

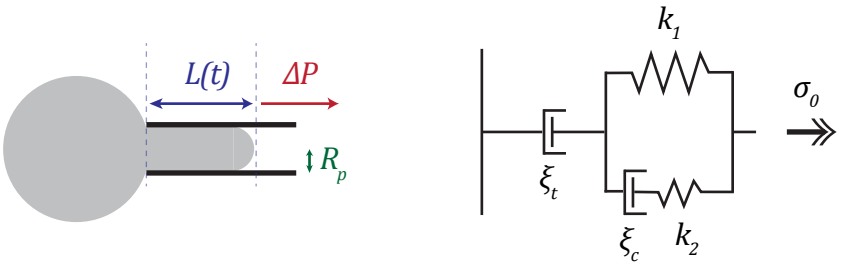

Additional Supplementary Figure:
Rheological model used in the micropipette aspiration assay.

Where $L(t)$ is the advancement of the aspirated cell in the pipette, given by :

$$L(t) = \frac{\sigma_0}{k_1}\left(1 - \frac{k_2}{k_1 + k_2} e^{(-t/\tau_c)}\right) + \frac{\sigma_0}{\xi_t} t$$

With σ_0 the constraint applied at the surface of the cell for triggering the aspiration inside the capillary, given by $\sigma_0 = \frac{2R_p \Delta P}{\pi}$, where R_p is the radius of the capillary opening (3.5 µm) and ΔP is the pressure differential given by $\Delta P = \rho g \Delta h$, where ρ is the density of PBS (1000 g/L), g represents gravitational acceleration (9.81 m/s^2) and Δh is the vertical displacement applied to the PBS column during aspiration (10.5 cm). τ_c refers to the relaxation time. k_1 is used to account for cell elasticity as it is the spring constant related to the elasticity of the cell and is directly linked to the elastic modulus E through $k_1 = \pi R_p E$. ξ_t is used to account for cell viscosity as it represents the viscous dissipation of the cell and is directly linked to the viscosity η through $\xi_t = 3\pi^2 \eta R_p$.

Supplementary References

47. Janmey, P. A., Georges, P. C. & Hvidt, S. Basic rheology for biologists. *Methods Cell Biol* **83**, 3–27 (2007).
48. Reichel, F., Goswami, R., Girardo, S. & Guck, J. High-throughput viscoelastic characterization of cells in hyperbolic microchannels. *Lab Chip* **24**, 2440–2453 (2024).
49. Taubenberger, A. V. *et al.* 3D Microenvironment Stiffness Regulates Tumor Spheroid Growth and Mechanics via p21 and ROCK. *Adv Biosyst* **3**, e1900128 (2019).
50. Zhang, S. *et al.* Intravital measurements of solid stresses in tumours reveal length-scale and microenvironmentally dependent force transmission. *Nat. Biomed. Eng* **7**, 1473–1492 (2023).
51. Urbanska, M. & Guck, J. Single-Cell Mechanics: Structural Determinants and Functional Relevance. *Annu Rev Biophys* **53**, 367–395 (2024).
52. Vahabikashi, A. *et al.* Nuclear lamin isoforms differentially contribute to LINC complex-dependent nucleocytoskeletal coupling and whole-cell mechanics. *Proc Natl Acad Sci U S A* **119**, e2121816119 (2022).
53. Janmey, P. A., Euteneuer, U., Traub, P. & Schliwa, M. Viscoelastic properties of vimentin compared with other filamentous biopolymer networks. *J Cell Biol* **113**, 155–160 (1991).
54. Lolo, F.-N. *et al.* Caveolin-1 dolines form a distinct and rapid caveolae-independent mechanoadaptation system. *Nat Cell Biol* **25**, 120–133 (2023).
55. Chugh, P. & Paluch, E. K. The actin cortex at a glance. *J Cell Sci* **131**, jcs186254 (2018).
56. Urbanska, M. *et al.* De novo identification of universal cell mechanics gene signatures. *eLife* **12**, RP87930 (2025).
57. Aceto, N. *et al.* Circulating tumor cell clusters are oligoclonal precursors of breast cancer metastasis. *Cell* **158**, 1110–1122 (2014).
58. Nazarian, R. *et al.* Melanomas acquire resistance to B-RAF(V600E) inhibition by RTK or N-RAS upregulation. *Nature* **468**, 973–977 (2010).

59. Entenberg, D. *et al.* In vivo subcellular resolution optical imaging in the lung reveals early metastatic proliferation and motility. *Intravital* **4**, 1–11 (2015).
60. Lam, C. K., Yoo, T., Hiner, B., Liu, Z. & Grutzendler, J. Embolus extravasation is an alternative mechanism for cerebral microvascular recanalization. *Nature* **465**, 478–482 (2010).
61. Massagué, J. & Ganesh, K. Metastasis-Initiating Cells and Ecosystems. *Cancer Discov* **11**, 971–994 (2021).
62. Grasset, E. M. *et al.* Triple-negative breast cancer metastasis involves complex epithelial-mesenchymal transition dynamics and requires vimentin. *Sci Transl Med* **14**, eabn7571 (2022).
63. Bell, E. S. *et al.* Low lamin A levels enhance confined cell migration and metastatic capacity in breast cancer. *Oncogene* **41**, 4211–4230 (2022).
64. Harada, T. *et al.* Nuclear lamin stiffness is a barrier to 3D migration, but softness can limit survival. *J Cell Biol* **204**, 669–682 (2014).
65. Coelho-Rato, L. S., Parvanian, S., Andrs Salajkova, S., Medalia, O. & Eriksson, J. E. Intermediate filaments at a glance. *J Cell Sci* **137**, jcs261386 (2024).
66. Kalukula, Y., Stephens, A. D., Lammerding, J. & Gabriele, S. Mechanics and functional consequences of nuclear deformations. *Nat Rev Mol Cell Biol* **23**, 583–602 (2022).
67. Lv, J. *et al.* Cell softness regulates tumorigenicity and stemness of cancer cells. *EMBO J* **40**, e106123 (2021).
68. Handler, C., Testi, C. & Scarcelli, G. Advantages of integrating Brillouin microscopy in multimodal mechanical mapping of cells and tissues. *Current Opinion in Cell Biology* **88**, 102341 (2024).
69. Osmani, N. *et al.* Probing Intravascular Adhesion and Extravasation of Tumor Cells with Microfluidics. *Methods Mol Biol* **2294**, 111–132 (2021).
70. Andrews, S. Babraham Bioinformatics - FastQC A Quality Control tool for High Throughput Sequence Data. https://www.bioinformatics.babraham.ac.uk/projects/fastqc/.
71. Dobin, A. *et al.* STAR: ultrafast universal RNA-seq aligner. *Bioinformatics* **29**, 15–21 (2013).
72. Liao, Y., Smyth, G. K. & Shi, W. featureCounts: an efficient general purpose program for assigning sequence reads to genomic features. *Bioinformatics* **30**, 923–930 (2014).

73. Love, M. I., Huber, W. & Anders, S. Moderated estimation of fold change and dispersion for RNA-seq data with DESeq2. *Genome Biol* **15**, 550 (2014).
74. Gentleman, R. C. *et al.* Bioconductor: open software development for computational biology and bioinformatics. *Genome Biol* **5**, R80 (2004).
75. Ritchie, M. E. *et al.* limma powers differential expression analyses for RNA-sequencing and microarray studies. *Nucleic Acids Res* **43**, e47 (2015).
76. Alsteens, D. *et al.* Nanomechanical mapping of first binding steps of a virus to animal cells. *Nat Nanotechnol* **12**, 177–183 (2017).
77. Fläschner, G., Roman, C. I., Strohmeyer, N., Martinez-Martin, D. & Müller, D. J. Rheology of rounded mammalian cells over continuous high-frequencies. *Nat Commun* **12**, 2922 (2021).